



City Research Online

City St George's, University of London

Citation: du Puits, R. & Bruecker, C. (2020). Fluctuations of the wall shear stress vector in a large-scale natural convection cell. *AIP Advances*, 10(7), 075105. doi: 10.1063/5.0006610

This is the accepted version of the paper.

This version of the publication may differ from the final published version. To cite this item please consult the publisher's version.

Permanent repository link: <https://openaccess.city.ac.uk/id/eprint/24383/>

Link to published version: <https://doi.org/10.1063/5.0006610>

Copyright and Reuse: Copyright and Moral Rights remain with the author(s) and/or copyright holders. Copies of full items can be used for personal research or study, educational, or not-for-profit purposes without prior permission or charge, unless otherwise indicated, provided that the authors, title and full bibliographic details are credited, a hyperlink and/or URL is given for the original metadata page and the content is not changed in any way. For full details of reuse please refer to [City Research Online policy](#).

Fluctuations of the wall shear stress vector in a large-scale natural convection cell

R. du Puits¹, C. Bruecker,^{2,a)}

¹ *Institute of Thermodynamics and Fluid Mechanics, Technische Universitaet Ilmenau, 98684 Ilmenau, Germany*

² *School of Mathematics, Computer Science and Engineering, City, University of London, London EC1V 0HB, UK*

We report first experimental data of the wall shear stress in turbulent air flow in a large-scale Rayleigh-Bénard experiment. Using a novel, nature-inspired measurement concept (Bruecker and Mikulich 2017, PLoS ONE 12, e0179253), we measured the mean and fluctuating part of the two components of the wall shear stress vector at the heated bottom plate at a Rayleigh number $Ra=1.58e10$ and a Prandtl number $Pr=0.7$. The total sampling period of 1,5 hours allowed to capture the dynamics of the magnitude and the orientation of the vector over several orders of characteristic time-scales of the large-scale circulation. We found the amplitude of short-term (turbulent) fluctuations to be following a highly skewed Weibull distribution, while the long-term fluctuations are dominated by the modulation effect of a quasi-regular angular precession of the outer flow around a constant mean, the time-scale of which is coupled to the characteristic eddy turn-over time of the global recirculation roll. Events of instantaneous negative streamwise wall shear occur when rapid twisting of the local flow happens. A mechanical model is used to explain the precession by tilting the spin moment of the large circulation roll and conservation of angular momentum. A slow angular drift of the mean orientation is observed in a phase of considerable weakening of mean wind magnitude.

^{a)} corresponding author: christoph.bruecker@city.ac.uk

1 I. INTRODUCTION

2 Since Ludwig Prandtl's pioneering work, we know that the local heat transport at a surface
3 with a temperature differing from that of the surrounded fluid is linked to the local momentum
4 transport across the fluid layer close to the surface¹. Measurements of the local wall shear stress
5 (WSS) may, therefore, contribute to a better understanding of the convective heat transfer process.
6 However, that kind of data reflecting the dynamics of the local heat/momentum transport is rare,
7 and to our knowledge, the present work is the first one providing measurement data of the
8 instantaneous two-dimensional (2-D) vector of the local WSS in thermal convection.

9 Following Prandtl's idea, Ludwig carried out a first analysis of the relation between the heat and
10 momentum transport in thermal convection. Unfortunately, he did not have the appropriate metrology,
11 and he could obtain only the time-averaged WSS from measurements of the profile of the velocity
12 parallel to the wall². For large-scale air convection studies such as in the so-called "Barrel of Ilmenau"
13 (BOI), the existing data base is still limited to mean velocity profile measurements from which only a
14 single component of the mean WSS could be derived. Due to the lack of sufficiently sensitive sensors
15 of the WSS, the current status quo in such data knowledge is therefore solely available from Direct
16 Numerical Simulations (DNS). Such simulations provide the local WSS vector information in time, but
17 usually for a limited simulation period of only a few tens of minutes. First simulation data, published
18 by Scheel and Schumacher³ show the existence of singularities in the wall shear stress vector field
19 similar as those reported in Bruecker⁴. These singularities are considered as footprints of large eruptions
20 of fluid parcels from the wall, who significantly affect the heat transport⁵. It is, therefore, the authors'
21 conclusion that information on the magnitude and the angle of the WSS vector as well as information
22 on its temporal behavior are crucial to understand the local momentum and heat transport processes at
23 the wall.

24 In order to measure the instantaneous WSS in low-speed air flows, Bruecker and Mikulich
25 developed a novel sensor, which was particularly designed to be used in large-scale convection air flows
26 such as in the Barrel of Ilmenau⁶. As the authors of the paper report, the sensitivity and the dynamic
27 response of the sensor, which is based on a nature-grown Dandelion pappus, were sufficiently good
28 to resolve the dynamics of the very small WSS in thermal convection in air. The present work reports
29 the first application of this sensor in a large-scale convection experiment in the BOI. It addresses the
30 hitherto unknown dynamics of the WSS by simultaneously measuring the magnitude and the direction
31 of the WSS vector. The results display the behavior of the modulation of the local WSS by the outer
32 main wind and give insight into the statistics and dynamics of the turbulent boundary layer.

33 The paper is organized as follows: In Section 2, we describe the essentials of the measurement
34 technology as well as the convection experiment wherein the sensor has been applied. Section 3
35 contains the results of our measurements and in Section 4, we summarize our discussion.

36

37 **II. EXPERIMENTAL SET-UP AND MEASUREMENT TECHNIQUE**

38 **A. The large-scale Rayleigh-Bénard experiment "Barrel of Ilmenau"**

39 The WSS measurements were carried out in the so-called "Barrel of Ilmenau (BOI)" a Rayleigh-Bénard
40 (RB) experiment using air ($Pr = 0.7$) as working fluid (see Fig. 1) and with the sensor mounted at the
41 center of the bottom plate. The BOI consists of a virtually adiabatic container of cylindrical shape with
42 an inner diameter of $D = 7.15$ m. A heating plate at the lower side releases the heat to the air layer, and
43 a cooling plate at the upper side removes it. Both plates are carefully levelled perpendicular to the vector
44 of gravity with an uncertainty of less than 0.15 degrees. The thickness of the air layer H can be varied
45 continuously between $0.15 \text{ m} < H < 6.30 \text{ m}$ by moving the cooling plate up and down. The
46 temperature of both plates can be set to values between $20^\circ\text{C} < T_h < 80^\circ\text{C}$ (heating plate) and $10^\circ\text{C} <$

47 $T_c < 30^\circ\text{C}$ (cooling plate). Due to the specific design of both plates (for more details see du Puits et
 48 al.⁷), the temperature at their surfaces is very uniform and the deviation does not exceed 1.5 % of the
 49 total temperature drop $\Delta T = T_h - T_c$ across the air layer.

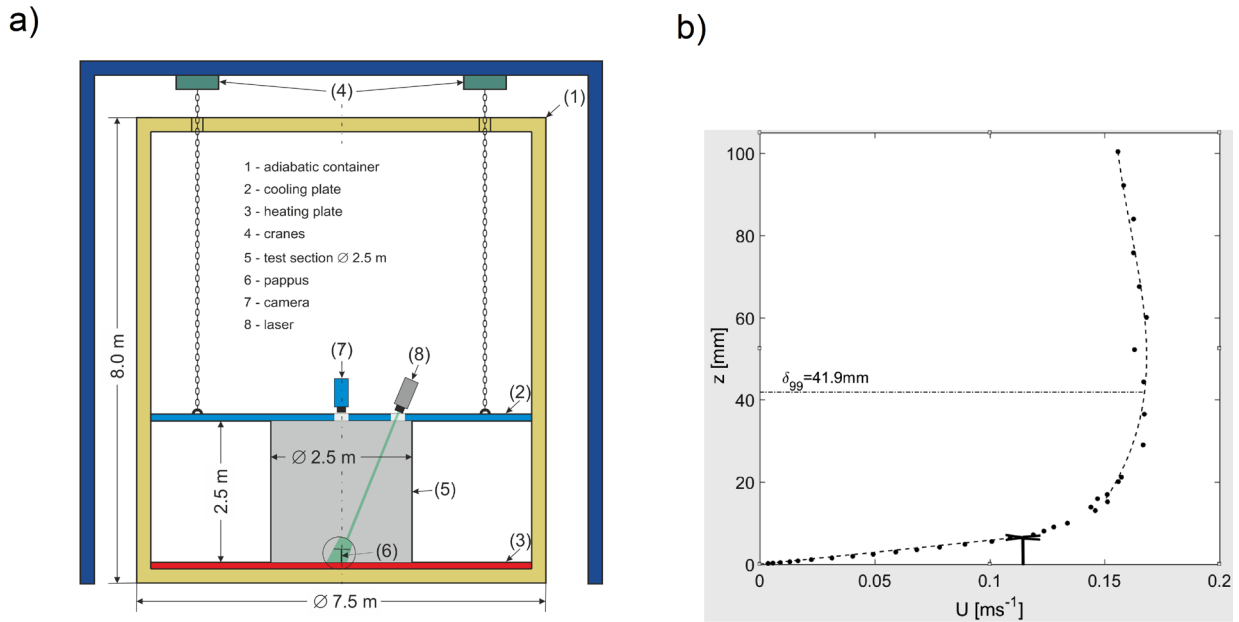


Figure 1a: Sketch of the large-scale Rayleigh-Bénard experiment “Barrel of Ilmenau” with the smaller inset of $D = 2.5\text{ m}$. The origin of a Cartesian coordinate system is fixed with the center of the bottom wall (the location of the wall shear stress sensor) in the x, y plane and the z axis pointing normal to the wall towards the top plate. Figure 1b: Mean velocity profile in the boundary layer of the BOI7 at the center of the cell. The plot shows the magnitude of the velocity vector at the centerline in different planes z parallel to the surface of the wall. Inserted is a true-scale sketch of the sensor with its head at $z_0 = 7\text{ mm}$, illustrating that it is fully surrounded by the linear part of the velocity profile

50

51 The variation of the surface temperature over the time is even smaller and remains below $\pm 0.02\text{ K}$. The
 52 sidewall of the convection cell is equipped with an active compensation heating system that efficiently
 53 prevents a heat exchange between the interior of the RB cell and the environment. Glass windows in
 54 the top plate allow the optical access to the interior of the test section for the illumination and for taking
 55 recordings. For our measurements we used a smaller inset of diameter $D = 2.5\text{ m}$ and height $H =$
 56 2.5 m that was placed within the large-size test section (see also Fig. 1). The temperature at the bottom

57 heating plate was set to $T_h = 25^\circ\text{C}$ and at the top cooling plate to $T_c = 15^\circ\text{C}$, thus providing a
 58 temperature difference of $\Delta T = 10\text{ K}$. The Rayleigh number $Ra = (\beta g \Delta T H^3) / (\nu \kappa)$ under these
 59 conditions is $Ra = 1.58 \cdot 10^{10}$, with the thermal expansion coefficient $\beta = 3.421\text{e-}3\text{ K}^{-1}$, the
 60 gravitational acceleration $g = 9.81\text{ ms}^{-2}$, the kinematic viscosity $\nu = 1.532\text{e-}5\text{ m}^2\text{s}^{-1}$ at 20° , and the
 61 thermal diffusivity $\kappa = 2.163\text{e-}5\text{ m}^2\text{s}^{-1}$. The particular benefit of the inset configuration is the fact that
 62 the vertical temperature distribution inside and outside the inset equals, therefore the sidewall can be
 63 considered as fully adiabatic. The characteristic timescale of the flow in the test section is the so-called
 64 free-fall time unit, defined as $T_f = \sqrt{\beta g \Delta T H}$, which is about $T_f = 2.7\text{ s}$ for the current configuration.
 65 Another timescale is the characteristic eddy turnover time T_e of the large circulation cell (LSC) in form
 66 of a single recirculation roll, which is calculated from the mean wind $U = 0.15\text{ ms}^{-1}$ and the
 67 circumference of the cell to about $T_e = 50\text{ s}$.

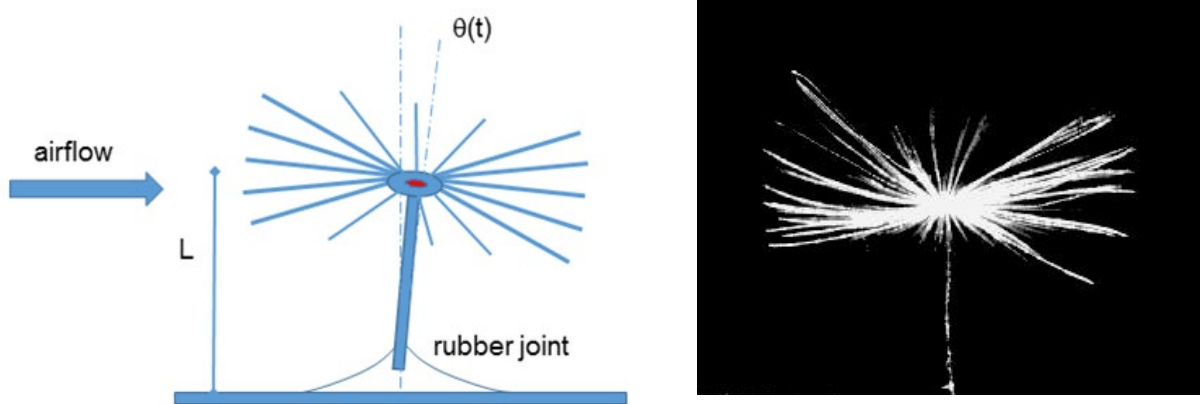


Figure 2: Principle of the measurement concept using a wall-mounted cantilever beam with a pappus head (left). Pictures of the pappus sensor fixated with the stem in the flexible membrane at the bottom plate of the BOI (right).

68

69 **The wall shear stress sensor**

70

71 The sensor including its calibration in the BOI is described in detail in Bruecker and Mikulich⁶. It

72 follows the principle of an indirect WSS measurement by calculating the near-wall velocity gradient
 73 from the wall-parallel velocity at a given (short) distance from the wall. It is based on the flow-induced
 74 deflection of an elastically-mounted cantilever beam (inverted pendulum) that is built at his head from
 75 a pappus of micro-hairs (nature-grown Dandelion pappus) (Fig. 2). To maximize the sensitivity, the
 76 sensor's head consists of a pappus of slender hairs with a diameter of a few tens of microns, acting as an
 77 antenna. The mechanical behavior of the sensor is described in Bruecker and Mikulich⁶ as a forced
 78 system with second-order response in overdamped condition (overdamped harmonic oscillator). A
 79 calibration of the mechanical model can provide the two unknown variables of the solution to the
 80 response function, the constant gain K and the cut-off frequency f_c , the frequency at which the sensor
 81 can no longer follow the excitation. A detailed view of the sensor is shown in Fig. 2. The stem and head
 82 were taken from a nature-grown Dandelion with a pappus of radially arranged slender hairs (mean
 83 length $l = 7$ mm, mean diameter $d = 30 \mu\text{m}$)⁶. It has a stem height of $z_0 = 7$ mm and the overall
 84 radial diameter of the pappus is about $D_p = 14$ mm. The Reynolds number Re of the flow around the
 85 individual hairs - simplified as thin cylinders of diameter d - is of the order of $Re_d \approx 2$ for air speeds
 86 of 1 ms^{-1} . Thus, the drag is dominated by viscous friction and it scales, therefore, approximately linear
 87 with the flow speed⁸⁻¹⁰. The elastic joint, at which the stem's foot is bonded, is made from rubber silicone
 88 (Polydimethylsiloxane, PDMS; Youngs modulus $E \approx 1.5$ MPa) and acts as a linear-elastic torsional
 89 spring with uniform bending stiffness in radial direction. When the stem with the pappus is exposed to
 90 an air flow parallel to the wall, the resulting torque tilts the stem around the joint, similar to an inverted
 91 pendulum. As the tilt is proportional to the torque, the latter can be measured indirectly by the end-to-
 92 end shift vector $\vec{Q}(t)$ of the tip relative to the wind-off reference. We capture the tilting motion of the
 93 pappus by imaging it's orbital motion from top, which provides the projection of the tip's end-to-end
 94 vector in the horizontal x, y plane at $z = z_0$ with $\vec{Q}_{x,y}(t) = [Q_x(t), Q_y(t)]$. For small tilt angles and

95 a sufficiently small sensor scale with $z_0 \ll \delta$, these quantities are directly proportional to the wall shear
 96 stress components $\tau_{x,y}$ (see also in Skupsch et al.¹¹). In 3D flows the wall shear stress is a vector $\vec{\tau}(t) =$
 97 $[\tau_x(t), \tau_y(t)]$, respectively the streamwise and the spanwise component (assuming the mean flow
 98 parallel to the wall in x-direction). Both components are defined by the wall-normal velocity gradients
 99 $\partial u_x / \partial z|_{z=0\text{mm}}$ and $\partial u_y / \partial z|_{z=0\text{mm}}$ at the wall (in the plane perpendicular to the wall-normal
 100 coordinate z). Using a Taylor expansion, the information of the velocity field in the x, y plane close to
 101 the wall at a distance $z = z_0$ is related to the wall shear stress as follows¹²:

$$102 \quad \tau_{x,y} = \mu \frac{u_{x,y}(z_0)}{z_0} + O(z_0)^2 \quad (1)$$

103 with

$$104 \quad u_{x,y}(z_0) \approx K Q_{x,y} \quad (2)$$

105 The second order term in Eq. 1 can be neglected in the viscous-dominated near-wall region (viscous
 106 sublayer). Previous flow studies in the BOI using Laser Doppler Velocimetry show a typical profile of
 107 the mean velocity at the position of the sensor, measured using Laser Doppler Velocimetry, see Fig. 1.
 108 The linear part of the profile as indicated by the dashed line represents the viscous sublayer close to the
 109 wall. The picture additionally displays a true-scale sketch of the sensor, which illustrates that the sensor
 110 is at the edge of the linear regime. Measurements by Ampofo and Karayiannis¹⁶ in a similar low-
 111 turbulence convection flow as studied herein show that the viscous sublayer thickness is of order of
 112 10 % of the outer boundary layer, similar as observed in the BOI. The constant gain K in Eq. 2 was
 113 measured in-situ using a wind-generating device placed inside the BOI under isothermal conditions (see
 114 Fig. 3). The air flow is generated with a planar nozzle that generates a Blasius-type wall-jet at the
 115 location of the sensor 20 slot heights h_s away (Brücker & Mikulich 2017). Different jet velocities up to
 116 $v = 1.50 \text{ ms}^{-1}$ have been set and the deflection $\vec{Q}_{x,y}$ of the sensor head was measured.

117 The results of the calibration procedure show a proportional increase of $\vec{Q}_{x,y}$ with the velocity of the
 118 Blasius jet at z_0 . Recalling that a linear relationship is expected between air velocity and pappus drag a
 119 linear regression is applied to the measurements for the interesting range of velocities $< 0.8\text{m/s}$, which
 120 provides the gain $K = 1000 \text{ s}^{-1}$ with the standard error of 5%.

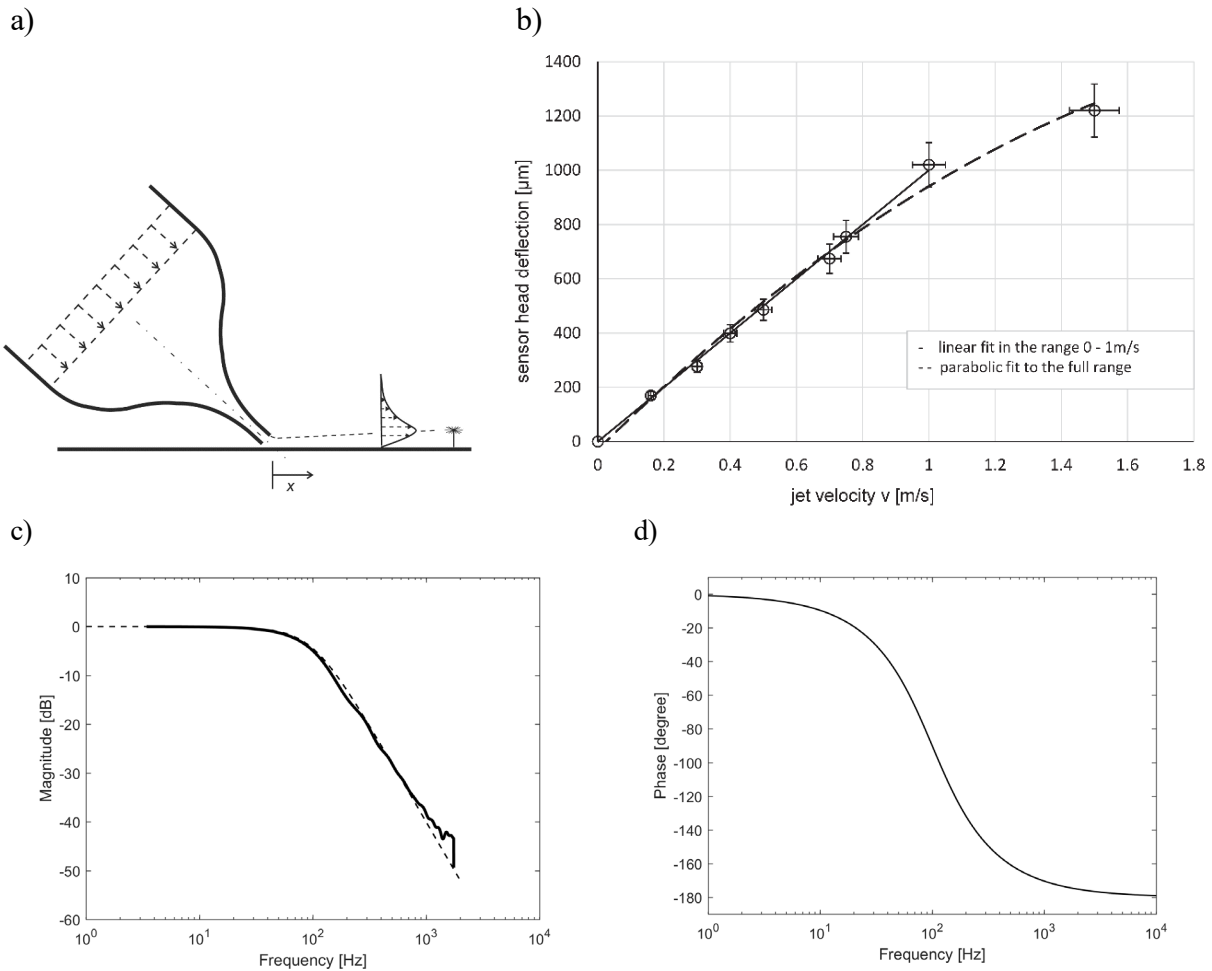


Figure 3: Sketch of the wall-jet apparatus a) for static sensor calibration shown in b). The dynamic response was measured with a step-response test with the magnitude and phase given in c) and d), respectively. The dashed line in c) indicates the theoretical response of a second-order critically damped system fitted to the measured parameters

121

122 Beyond a velocity of about 0.8 ms^{-1} , the recordings show that the configuration of the hairs starts to
 123 change over time and the linear relationship is no longer valid. This critical value is never exceeded in

124 the convective airflow in the BOI. A step-response test with the sensor further provides the dynamic
125 response, given as the magnitude and phase of the transfer function, see Fig. 3c and 3d. The curves
126 match the response of a second-order critically damped mechanical oscillator from which one obtains
127 the cut-off frequency f_c , at which the sensor can no longer follow the signal (the response starts to roll-
128 off at -40 dB per decade). This is at a frequency of 100 Hz, which alternatively means a response time
129 of approximately about $\tau_{95} = 10$ ms in reverse. Since the typical time-scale of the smallest near-wall
130 fluctuations has been measured in the past with about 0.5 s^{15} , the sensor works completely in the range
131 of constant amplitude response (gain) and zero phase-shift in the measurement range of $f < 2\text{Hz}$, capable
132 to map the full dynamics of the flow.

133 **B. Optical set-up for sensor imaging**

134 The optical set-up for the tip-deflection measurements is shown in Fig. 1. The pappus sensor at the
135 bottom plate was illuminated by a defocused Laser beam (Raypower 5000, 5~W power at $\lambda = 532$ nm,
136 Dantec Dynamics, Skovlunde, Denmark) expanded to illuminate a spot of 50 mm diameter at the floor.
137 A CCD camera (mvBlueFOX3-1031, Matrix Vision, Oppenweiler, Germany) placed on top of the
138 cooling plate acquires the deflection of the sensor head in the wall-parallel x, y plane with a resolution
139 of $2048 \times 1536 \text{ px}^2$ and a frame rate of 10 Hz. The camera is equipped with a long-distance microscope
140 (model K2/SCTM, Infinity Photo-Optical, Goettingen, Germany), which provides a resolution of
141 185 px/mm . A total number of 54,000 images was recorded in a single measurement campaign. The
142 images are streamed via USB~3 to the hard disc of a desktop. This equates to a maximum of 1.5~hours
143 of observation time per experiment. To avoid any vibrations during the recordings, the facility was left
144 alone after starting the recording and no external disturbance could enter the RB cell. In order to remove
145 any vibration induced by leaving and re-entering the facility, the first and the last 2-3 minutes were
146 rejected before we analysed the data.

147 The tip displacement vector in the images is obtained using a 2-D cross-correlation method similar
 148 as in Particle Image Velocimetry technique¹⁷, where we compare the quadratic subsection of the sensor
 149 image between wind-off and wind-on situation. The shift in tip position relative to wind-off is
 150 determined with subpixel accuracy using a 3-point Gaussian fit of the correlation peak in x- and y-
 151 direction, which has an uncertainty of about 0.05 px. A reference marker on the floor is used to correct
 152 for potential vibrations of the camera during the recordings. After multiplication of the shift with the
 153 lens magnification, the vector $\vec{Q}_{x,y}(t)$ of the sensor head is recovered for each time-step in the image
 154 sequence.

155 In order to make our data comparable with velocity-gradient data recently obtained from PIV
 156 measurements, we consider in the following the viscosity-divided WSS $\tau_{x,y}/\mu$ (known as the wall-
 157 shear rate) with the two components:

$$158 \quad \tau_x(t)/\mu = KQ_x(t)/z_0$$

$$159 \quad \tau_y(t)/\mu = KQ_y(t)/z_0 \quad (3)$$

160 and we define the direction and the magnitude of the WSS as follows:

$$161 \quad \Phi(t) = \text{atan}(\tau_y(t)/\tau_x(t))$$

$$162 \quad \Psi(t) = \frac{1}{\mu} \|\tau\| = \frac{1}{\mu} \sqrt{\tau_x^2(t) + \tau_y^2(t)} \quad (4)$$

163 We capture our data with a sampling frequency of 10 Hz. In order to remove outliers, the data was
 164 filtered in time with a fourth-order Butterworth low-pass filter designed with a -3 dB cutoff frequency
 165 at 2 Hz. We have selected this particular frequency, since the typical time-scale of the smallest near-
 166 wall fluctuations has been measured in the past with about 0.5 s¹⁵. Our long-term recording of totally
 167 54,000 samples covers more than 100 LSC turnover times T_e , and ensures sufficient statistical evidence

168 even for the long timescales.

169

170 **III. Results and Discussion**

171 Preceding the discussion, it is worth to note that earlier studies in the barrel with a similar
172 aspect ratio indicate the existence of only a single LSC roller, which was observed also to perform
173 angular oscillations around a mean direction. The normal flow mode present in the BOI is where
174 the mean orientation of the LSC is locked in one particular direction. Because of the modulation
175 effect, which the outer flow enforces on the signal on the floor, the WSS signals should also reveal
176 the footprint of this wiggling motion. Fig. 4a and b show the complete time trace of the direction
177 $\Phi(t)$ and the magnitude $\Psi(t)$ of the WSS (viscosity-divided WSS $\tau_{x,y}/\mu$) over a period of
178 1.5 hours. Overlaid in color is the low-pass filtered data $\tilde{\Phi}_{LSC}$ and $\tilde{\Psi}_{LSC}$ (4th order Butterworth low-
179 pass filter designed with a -3 dB cut-off frequency at 0.003 Hz), based on the notation used in Shi et
180 al.¹⁸ Therefore, turbulent events happening close to the wall are filtered out (higher frequency) while
181 the footprint of fluctuations of the mean wind direction and magnitude of the LSC remain.

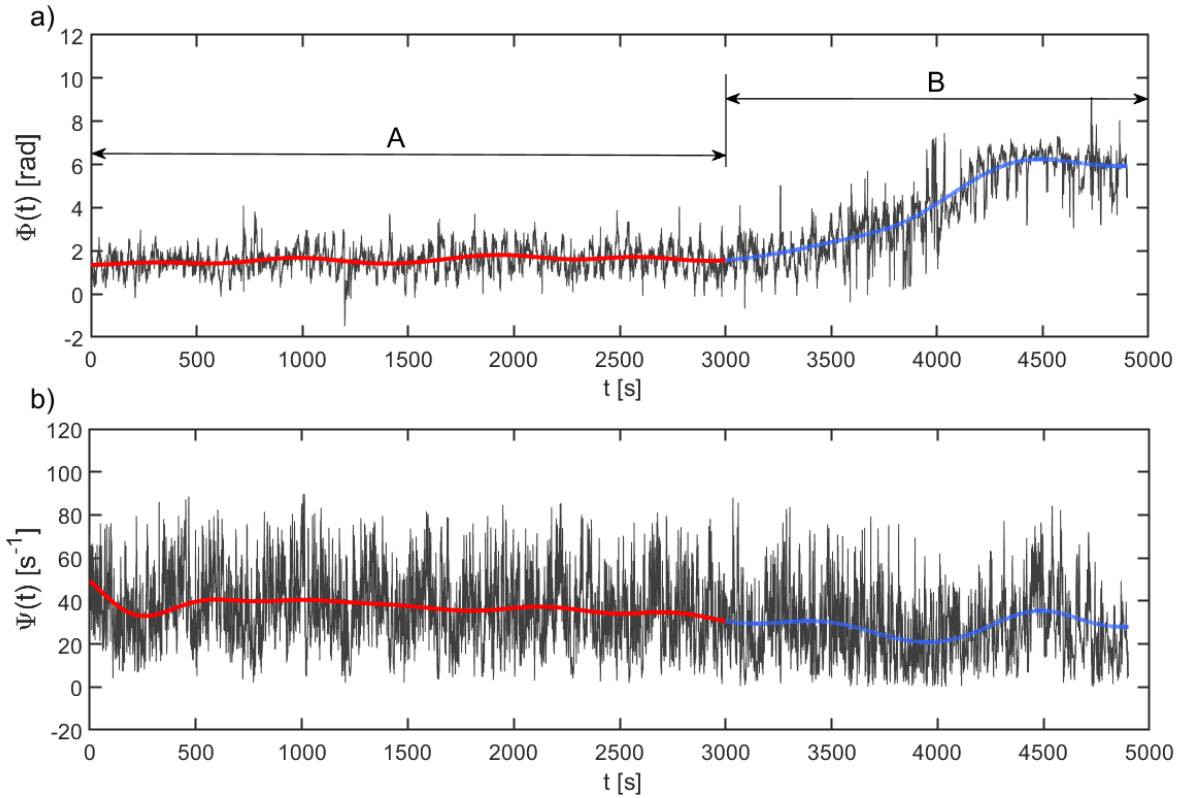


Figure 4: a) Plot of direction $\Phi(t)$ and b) magnitude $\Psi(t)$ of τ/μ over a period of 1.5 hours. Overlaid in color is the profile of the time-filtered signal of the direction $\tilde{\Phi}(t)$ and the magnitude $\tilde{\Psi}(t)$. Two different characteristic phases are coded in color (phase A in red, phase B in blue).

182

183 Both of the original data, the direction $\Phi(t)$ and magnitude $\Psi(t)$ of the WSS vector, fluctuate
 184 over time at a high frequency. Meanwhile, the low-pass filtered WSS vector is almost perfectly aligned
 185 with the x-axis in phase A ($t = 0 \dots 3,000$ s). Beginning at $t = 3,000$ s, a phase of a very slow drift
 186 of the angle $\tilde{\Phi}_{LSC}$ in counter-clockwise direction is seen, see phase B ($t = 3,000 \dots 5,000$ s). This
 187 angular drift indicates a slow precession of the mean axis of the LSC, meanwhile the oscillations at
 188 higher frequencies persisted. Such a slow precession mode can replace the normal flow mode present
 189 in the BOI. Initially, at $t = 1,000$ s in phase A, the mean WSS magnitude amounts to $\bar{\Psi} = 40 \text{ s}^{-1}$.
 190 It decreases then slowly over a period of 2,000 s further down to $\bar{\Psi} = 30 \text{ s}^{-1}$ at the end of Phase A

191 ($= 3000$ s) and finally reaches, in a rather short period, a minimum of $\bar{\Psi} = 20 \text{ s}^{-1}$ at $t = 4,000$ s
 192 in phase B (see Fig. 4b). The final slow-down lasted only about 1,000 s (366 units of T_f), which is when
 193 the angle $\tilde{\Phi}_{LSC}$ changed by π . Fig. 5 illustrates the complex behaviour of the flow in the x, y plane as a
 194 trace plot of the original and low-pass filtered WSS vector. As discussed before, the mean direction of
 195 the LSC in phase A (the red part of the time-filtered signal in Fig. 4) was almost constant towards north
 196 (positive x -axis), while in phase B the plane of the LSC shows a nearly constant angular drift in counter-
 197 clockwise direction.

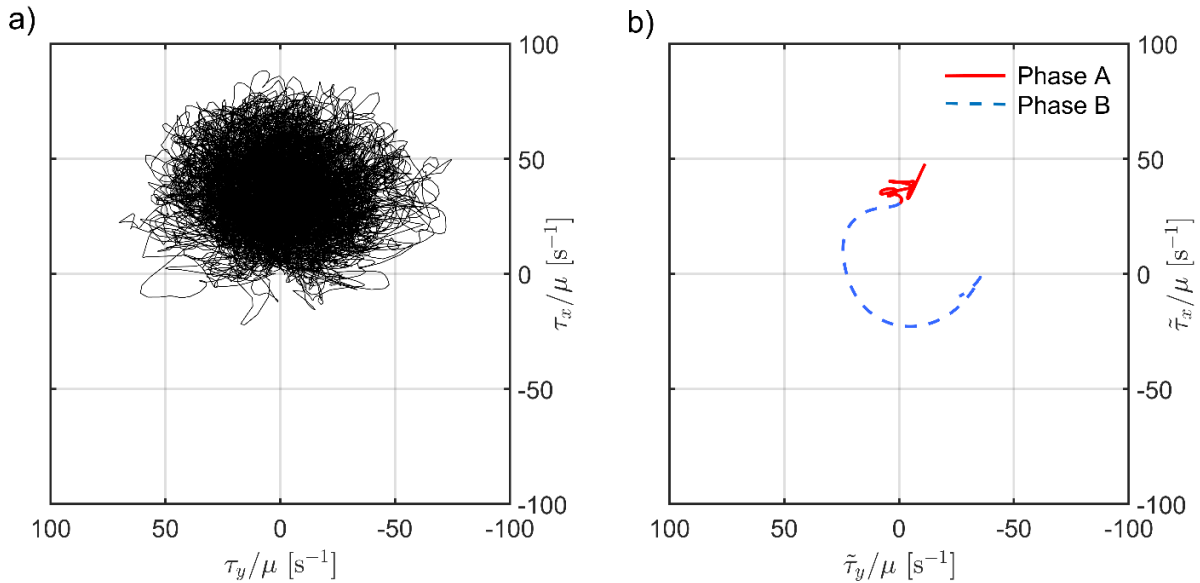


Figure 5: Time trace of the viscosity-divided WSS vector $\tau/\mu(t)$ in the x, y plane, comparable to the trace $Q(t)$ of the sensor head. a) $\tau/\mu(t)$ in phase A; b) time-filtered signal $\tilde{\tau}/\mu(t)$ in phase A (full red line) and in the successive phase B (dashed blue line).

198

199 When correlating the onset of the angular drift with the magnitude of the WSS, the data let us
 200 conclude that the mean axis of the LSC started to rotate at a time, when the magnitude of the main wind
 201 started to critically slow down. If we again follow the argument of the outer modulation effect, then the
 202 magnitude of the low-pass filtered WSS is proportional to the characteristic velocity of the LSC (mean

203 wind). From that, we can estimate the kinetic Energy \bar{E}_{kin} of the LSC as proportional to the square of
 204 the magnitude of the WSS with $\bar{E}_{kin} \sim \Psi^2$. The results show therefore that the average kinetic energy
 205 of the mean wind in phase B is reduced to about 50 % of the energy in phase A. Such a slow-down was
 206 also observed by du Puits et al.⁷ We hypothesize herein that the slow-down of the kinetic energy of the
 207 mean wind may have triggered the angular precession. The time scale of this precession is rather long,
 208 as it takes about 20 characteristic eddy turnovers of the LSC while the orientation drifts only along an
 209 angular arc of π .

210

211 We further analyze the temporal behavior of the magnitude Ψ and the angle Φ by computing their
 212 autocorrelation functions:

$$C_{xx}(\Delta t) = \lim_{n \rightarrow \infty} \frac{1}{n} \sum_{i=1}^n x_i(t) x_i(t + \Delta t) \quad (5).$$

213 We plot short in Fig. 6a and b exemplary short sequences of the time traces of $\Psi(t)$ and $\Phi(t)$
 214 together with the autocorrelation functions $C_{xx}(\Psi)$ and $C_{xx}(\Phi)$ calculated from the full data. While the
 215 oscillations of the magnitude $\Psi(t)$ seem to be rather irregular (see Fig. 6a), the plot of $\Phi(t)$ reveals a
 216 low frequency oscillation around the mean with a frequency of about 0.02 Hz (see Fig. 6b). This
 217 oscillatory variation of the orientation of the WSS angle $\Phi(t)$ over a range of more than ± 25 degrees is
 218 similar as already observed in Shi et al.¹⁸. The timescale related to this oscillation corresponds to the
 219 characteristic turnover time $T_e \approx 50$ s of the LSC. Its quasi-periodic nature is highlighted in the plot of
 220 the autocorrelation function $C_{xx}(\Phi)$ (see Fig. 6d), which shows strong periodic correlation peaks at
 221 multiples of the time-lag T_e (Fig. 6d). The dynamical system has obviously two attracting states in the
 222 orientation of the LSC overlaid with a certain fraction of noise/turbulence.²⁰

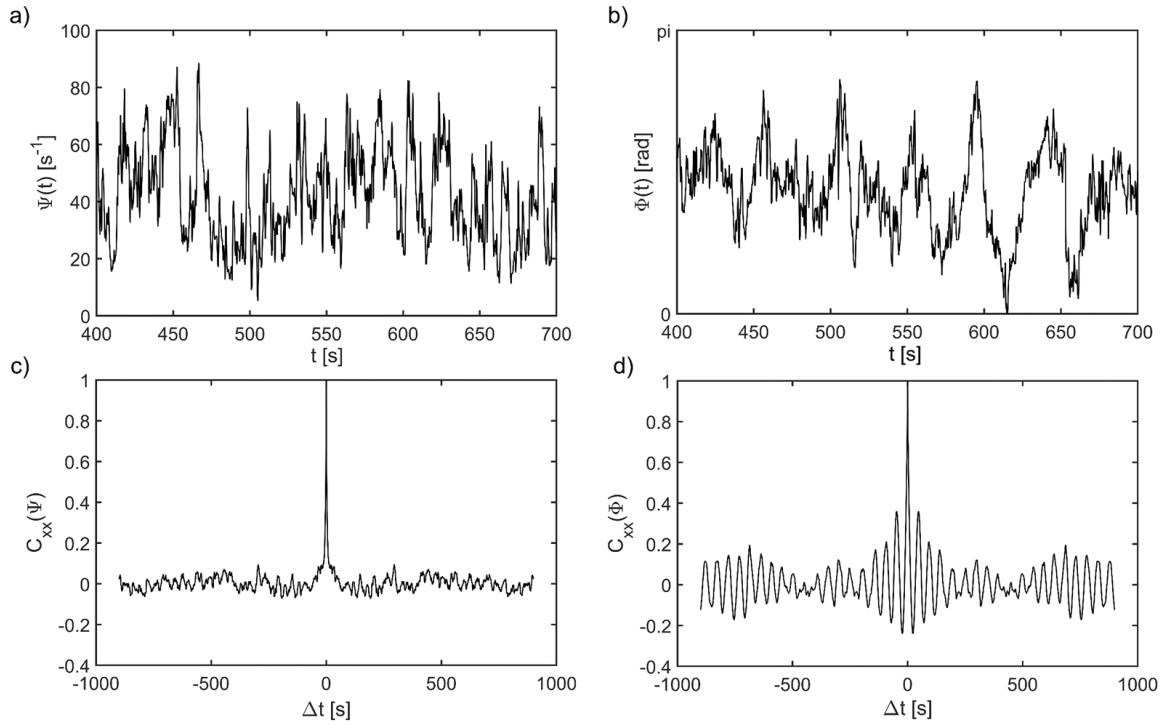


Figure 6: a,b) Time series of magnitude $\Psi(t)$ and direction $\Phi(t)$ of the wall shear stress vector τ/μ for phase A, $400 \text{ s} < t < 700 \text{ s}$; c,d) autocorrelation function of the magnitude $C_{xx}(\Psi)$ and the direction $C_{xx}(\Phi)$ for phase A.

223

224 Furthermore, the result shows a long-term modulation of the angular oscillations. The peak
 225 amplitude of the correlation slowly decreases for increasing time lag to about zero at a time lag of $\Delta t =$
 226 450 s (corresponds to $9T_e$) and then increases again to a local peak correlation value $C_{xx}(\Phi) = 0.2$ at
 227 $\Delta t = 700 \text{ s}$ ($14T_e$). The observed slow-down of the mean wind in phase B could be a consequence of
 228 this low-frequency modulation.

229 In the following, we exclusively focus on phase A when the mean direction of the wind is constant
 230 on a large time-scale and aligned with the x-axis with a mean WSS magnitude of $|\tau_x|/\mu = 35 \text{ s}^{-1}$
 231 and a rms of $\tau'_{x,rms}/\mu = 18.3 \text{ s}^{-1}$. An interesting feature is the observation of a negative streamwise
 232 wall shear stress τ_x as seen in the traces in Fig. 5a, when the line crosses the 2nd or 3rd quadrant in the

233 left sub-figure. Such events are observed in turbulent RB convection for the first time, but they were
 234 observed recently in turbulent boundary layer flows⁴.

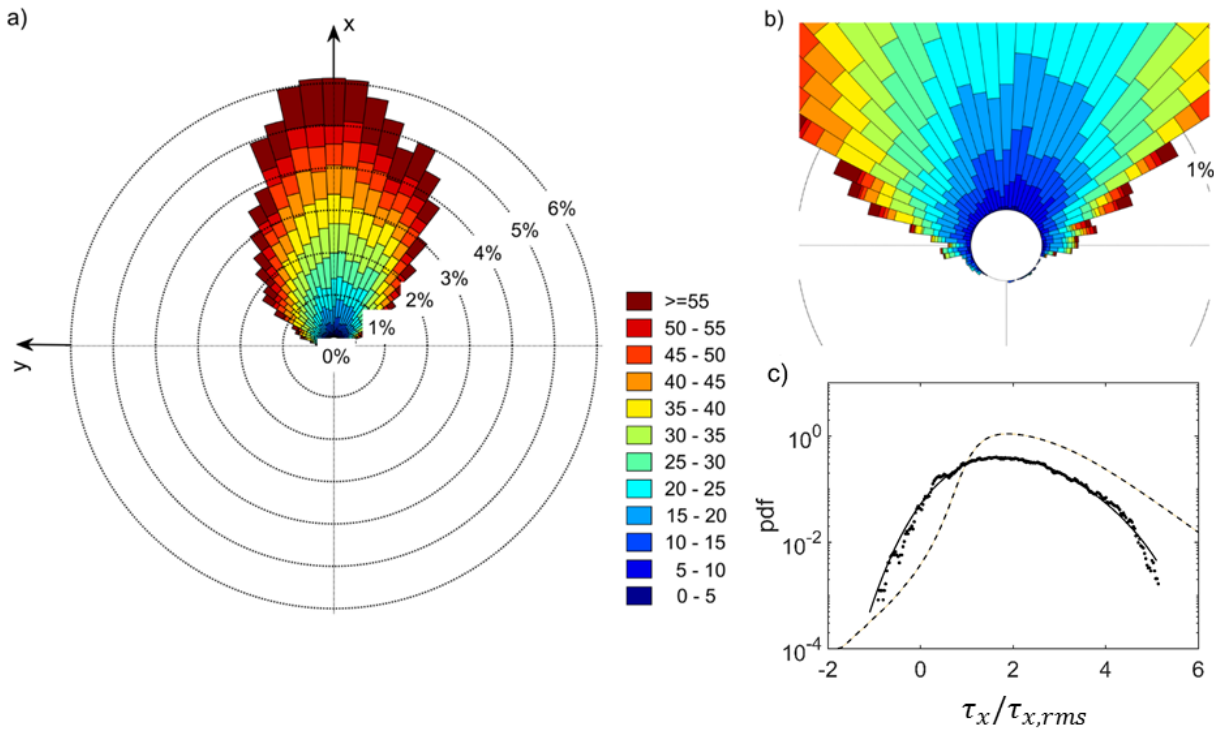


Figure 7: a) Polar plot of probability distribution of the wall-shear angle in phase A (mean wind flow is in x-direction). b) Zoom-in the image of the data given left. Angular steps are in 5 degrees. The color indicates the magnitude in the ranges given in the legend bar. c) Pdf of the streamwise wall shear stress normalized with its rms. The solid line represents the generalized extreme value distribution according to Eq. 6 and with the parameters given in the text. The dashed line shows the results from Örlü & Schlatter (2011) for a zero pressure-gradient turbulent boundary layer flow²⁵.

235
 236 Fig. 7 shows the angular probability density function of the yaw angle of the WSS as a wind rose
 237 plate with a mean direction towards north (x-axis). The angle Φ of the rays relative to north represent
 238 the yaw angle, while the length indicates the probability over all samples recorded in phase A. The
 239 magnitude Ψ is overlaid in colour. The graph is similar to that used by Bruecker displaying the
 240 measurements of the statistics of the wall shear stress in turbulent boundary layer (tbl) flows⁴. The
 241 distribution shows a type of cone, in which mean angles between ± 25 degrees around the x-axis

242 predominate. However, there are also, even rarely, events of τ , in which the yaw angle exceeds
 243 ± 90 degrees. Thus, these rare events can be associated with events of large spanwise τ_y , first argued in
 244 a zero-pressure-gradient tbl⁴. The probability and the yaw angle of the rare events in thermal convection
 245 are quite similar to those reported from tbl measurements. It however remains open if the origin of such
 246 events is the existence of quasi-streamwise vortices as argued in the case of tbl. The observation herein
 247 indicates a rapid temporal variation of the local direction of the fluctuating wall shear stress, representing
 248 a high angular velocity of the WSS vector τ during these events. Fig 7c shows the pdf of the streamwise
 249 WSS normalized with the rms. It demonstrates a non-symmetric distribution with prove of certain
 250 probability of negative streamwise WSS events. The measured PDFs shown in Fig. 7c can be well
 251 described by the generalized extreme value (GEV) distribution¹⁹.

$$P(x'; \lambda, k) = \frac{1}{\lambda} (1 + kx')^{-(1/k+1)} e^{-(1+kx')^{-1/k}} \quad (6)$$

252 where the variable $x' = (x - m)/\lambda$ with the shape parameter k , the scale parameter λ , and the location
 253 parameter m . The fit provides a shape parameter of $k = -0.1907$ ($\lambda = 0.937$, $m = 1.5403$).
 254 For $k < 0$, the distribution is reduced to the reversed Weibull distribution and has zero probability
 255 density for $x > -\lambda/(k + m)$. From the fitted values of x , we find the corresponding upper bound with
 256 $x > 6.4553$. Note that the herein observed distribution is reverse to the typical Weibull-type distribution
 257 observed in tbl, see the reference curve in Fig. 7c from Örlü & Schlatter (2011)²⁵. This means negative
 258 streamwise WSS events can have higher magnitude in convection flows.

259
 260 With respect to the occurrence of extreme events, it is quite difficult to analyse the data using
 261 classical conditional averaging methods or a fixed threshold definition due to this particular modulation
 262 of the magnitude and the orientation of the mean flow. Here, we try to discriminate the amplitude of the
 263 fluctuating WSS signals into separate timescales. We distinguish between the periodic transitive

264 dynamics represented in the low frequency dynamics of the mean wind and the small-scale turbulent
 265 fluctuations. To this end, we apply envelope functions with different time windows on τ_x to determine
 266 the amplitudes of these fluctuations on the different timescales. The envelope is calculated from the
 267 Matlab toolbox and uses a sliding time-window that connects within the window the local peaks (upper
 268 envelope for local maxima and lower envelope for local minimum peaks) with a smoothed spline²¹.

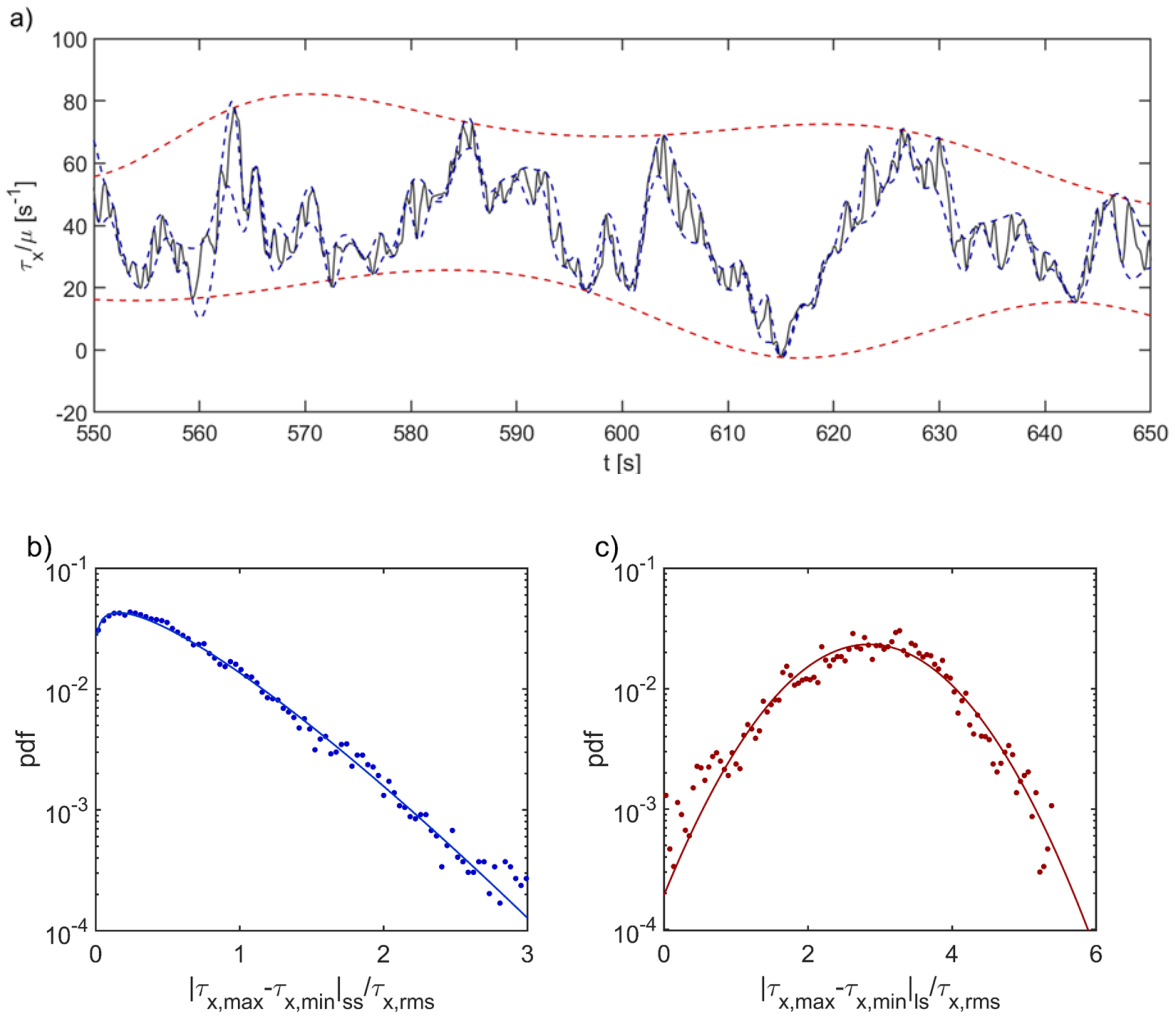


Figure 8: Peak-to-peak amplitude of the fluctuations of τ_x at different timescales. a) Time trace of τ_x (black line) with envelopes of the small-scale (ss) and large-scale (ls) fluctuations (thin blue and red lines, respectively). b) Probability density function (PDF) of the small-scale fluctuations (the solid line is a Weibull fit with a scale parameter $\lambda = 0.673$ and a shape parameter $k = 1.223$, c) PDF of the large-scale fluctuations (the solid line is a Gaussian fit with a mean value of $\bar{\tau}_x = 2.85$ and a standard deviation of $\sigma(\tau_x) = 0.92$)

270 For the low frequency dynamics, we chose a window of 15 s, while using a shorter time window
 271 of 0.5 s for the small-scale turbulent structures. One typical example of such an enveloping curve is
 272 plotted along with the original signal in Fig. 8a. In order to analyze the amplitude of the fluctuations,
 273 we compute the absolute difference between the upper and the lower envelopes $|\tau_{x,max} - \tau_{x,min}|$ and
 274 determine the probability density function (PDF) for both time windows (see Figs. 8b and c). The PDF
 275 of the small-scale (ss) fluctuations using a time window of 0.5~s is shown in Fig. 8b, that for the large-
 276 scale (ls) fluctuations is shown in Fig. 8c. While the ss fluctuations of the streamwise wall shear stress
 277 follow a Weibull distribution according to:

$$P(x; \lambda, k) = \frac{k}{\lambda} \left(\frac{x}{\lambda}\right)^{k-1} e^{-(x/\lambda)^k} \quad (7)$$

278 (with the scale parameter $\lambda = 0.637$ and the shape parameter $k = 1.223$), the ls fluctuations are clearly
 279 Gaussian distributed. The latter indicates a normal distribution of the amplitude of the angular
 280 fluctuations of the orientation of the LSC, as this contributes to the cyclic variation of τ_x . In conclusion,
 281 extreme events are more likely, if large excursions occur simultaneous for both statistical distributions.
 282

283 **IV. Conclusion**

284 We have presented and discussed the first measurements of the instantaneous wall shear stress in a
 285 large-scale Rayleigh-Bénard experiment at Rayleigh and Prandtl numbers $Ra = 1.58 \cdot 10^{10}$ and $Pr =$
 286 0.7 , respectively. Using a novel, nature-inspired pappus sensor, we measured the magnitude and the
 287 orientation of the local wall shear stress vector at the center of the heated bottom plate. The results of
 288 our 1,5 hours measurement series demonstrate that this vector undergoes strong fluctuations as well in
 289 its magnitude as in its orientation. Important to note is that the sensor signal at the wall represents the
 290 sum of both, the fluctuations on small time-scales due to the turbulent nature of the boundary layer, and

291 in addition the dynamics of the LSC due to the modulation effect of the outer flow onto the near-wall
 292 region. Therefore, our measurements allow also drawing conclusions on the magnitude and orientation
 293 of the main wind in the LSC. On average over a period of 3000s (phase A), the mean wind is almost
 294 perfectly aligned with the x-axis. However, we observe a clear quasi-periodic angular precession of the
 295 orientation of the LSC in the range 50-60° around the mean, each half-cycle taking exactly the time of
 296 one eddy turn-over time $T_e \approx 50$ s. The strong periodicity is manifested by the plot of the
 297 autocorrelation function $C_{xx}(\Phi)$, which shows periodic peaks at multiples of the eddy turn-over times
 298 with values larger than 0.2 even after more than 900 s (see Fig. 6d). Such a strong periodicity in the
 299 angular oscillations has not been observed so far and motivated us to illustrate the dynamics of the LSC
 300 in a simplified mechanical model for further discussion.

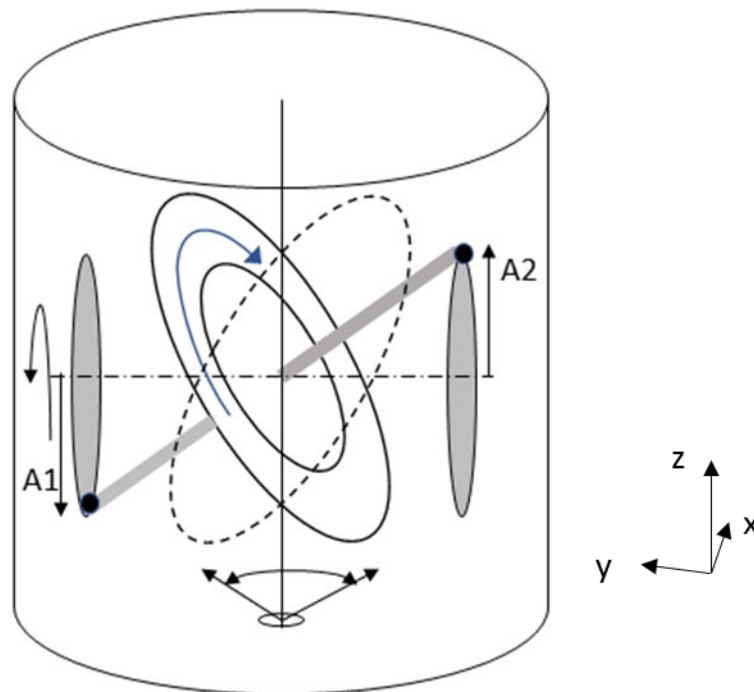


Figure 9: Simplified mechanical model of a tumbling rotating disc (tumbling LSC) to illustrate the modulation

effect on the quasi-periodic angular precession of the wall shear stress vector at the wall

301

302 A schematic mechanical model is illustrated in Fig. 9 to discuss the observed regular oscillations.

303 We hypothesize that the plane of the LSC with fluid rotating around its axis is represented by a rotating

304 disc, which axis is initially aligned horizontally with the y-axis. An initial disturbance in form of

305 asymmetric lateral down- and upwash at the sides of the LSC (A1-A2) cause a torque which tilts the

306 spin momentum of the LSC in the horizontal plane and leads to a self-enforcing of this asymmetry. As

307 the vortex axis reorients away from the horizontal plane, it generates a torque around the z-axis because

308 of conservation of angular momentum, which leads to a precession of the LSC. The cycle is reversed

309 when the front of the LSC – while precessing - reaches the region A2 and counteracts the upwash, while

310 the back of the LSC reverses the downwash A1. Hence, the system starts a cyclic clock-wise – counter-

311 clock wise precession motion around the z-axis, which correlates with the observed regular angular

312 oscillations of the orientation of the WSS vector. Note that the diagonal orientation of the LSC is not

313 contradicting previous observations that the orientation of the mean flow at the same instant and location

314 is different at the bottom plate compared to the top plate, supporting the idea of a tilted or twisted

315 circulation roll (Funfschilling & Ahlers 2004²³ ; Xi & Xia 2008²⁴).

316 The long-term recording also allowed us to detect a very slow drift of the mean orientation in a

317 certain phase (phase B) overlaid with the regular precessions described above. The angular drift in

318 counter-clockwise direction takes about 30 times the eddy turn-over time for a 270° turn. This slow

319 mode is accompanied by a decrease of the kinetic energy of the mean wind (imposed by the LSC) by

320 about 50 %. In the past, du Puits et al. reported at similar conditions also a critical weakening of the

321 mean wind for a period of four hours²². However, the authors could not link their observation to a

322 modification of the angular orientation of the global recirculation. A possible explanation for this slow

323 mode precession based on the proposed mechanical model could be a slight imbalance of the tumbling
324 cycle, which then leads to a net mean angular momentum. Transitional flow phenomena like the
325 reported rotation of the plane of the global recirculation has already been observed in turbulent
326 Rayleigh-Bénard convection (RBC) in the past, see ^{23,24}. However, they found that occur only very
327 rarely. Insofar, it was rather a lucky coincidence that we could observe such a transition in our 90
328 minutes long measurement.

329

330 Another phenomenon we observed in our long-term recordings is the occurrence of local backflow
331 in the boundary layer, while the large-scale circulation in phase A remains on average almost perfectly
332 aligned with the x-axis. Such local backflow events have also been detected recently in turbulent
333 boundary layer flow along a flat wall, but this is the first time that such events could be documented in
334 a temperature-gradient driven flow. Local backflow is correlated herein with large angular velocities of
335 the wall shear stress vector, which we understand as an indication for the existence of coherent vortical
336 structures with a large inclination of the axes against the wall (nearly wall-normal vortex funnels). These
337 short-term fluctuations have amplitudes which follow a highly skewed Weibull distribution, while the
338 amplitudes of fluctuations on the longer time scales are better fitted by a symmetric Gaussian. In both
339 distributions, the ends of the tails can reach amplitudes of 3-4 times the rms of the mean streamwise
340 wall shear stress. Such a coincidence of large values in both distributions indicates the high probability
341 of rare excursions of the near-wall flow, in magnitude as well in yaw angle.

342

343 **ACKNOWLEDGEMENTS**

344 The position of Professor Christoph Bruecker is co-funded as the BAE SYSTEMS Sir Richard
345 Olver Chair and the Royal Academy of Engineering Chair (grant RCSR1617/4/11) which is
346 gratefully acknowledged. We wish to acknowledge the support of the European Union under the
347 Grant Agreement number 312778 as well as the support from the German Research Foundation
348 under the grant number PU436/1-2 (the camera was sponsored in grant BR 1491/30-1). Moreover,
349 we thank Vladimir Mikulich, Sabine Abawi, and Vigimantas Mitschunas for their technical
350 assistance to run the experiment.

351

352 **DATA AVAILABILITY STATEMENTS**

353 Raw data were generated at the Ilmenau Barrel large-scale facility. Derived data supporting the
354 findings of this study are available from the corresponding author upon reasonable request.

355

356 **REFERENCES**

357 ¹ L. Prandtl, “Bericht ueber Untersuchungen zur ausgebildeten Turbulenz,“ Z. angew. Math.
358 Mech. 5, 136 (1925).

359 ² H. Ludwig, “Bestimmung des Verhaeltnisses der Austauschkoefizienten fuer Waerme und
360 Impuls bei turbulenten Grenzschichten, Z f. Flugwiss. 4, 73 (1956).

361 ³ J. D. Scheel, J. Schumacher, “Local boundary layer scales in turbulent Rayleigh-Bénard
362 convection,“ J. Fluid Mech. 758, 344 (2014).

363 ⁴ C. Bruecker, “Evidence of rare backflow and skin-friction critical points in near-wall turbulence
364 using micropillar imaging,“ Phys. Fluids 27, 031705 (2015).

- 365 ⁵ V. Bandaru, A. Kolchinskaya, K. Padberg-Gehle, J. Schumacher, “Role of critical points of the
366 skin friction field in formation of plumes in thermal convection,” *Phys. Rev. E* 92, 043006
367 (2015).
- 368 ⁶ C. Bruecker, V. Mikulich, “Sensing of minute airflow motions near walls using pappus-type
369 nature-inspired sensors,” *PLoS ONE* 12, e0179253 (2017).
- 370 ⁷ R. du Puits, C. Resagk, A. Thess, “Structure of viscous boundary layers in turbulent Rayleigh-
371 Bénard convection,” *New Journal of Physics* 15, 013040 (2013).
- 372 ⁸ E. Liebe, *Flow Phenomena in nature. A challenge to engineering design* (Wit
373 Press/Computational Mechanics, Southampton, 2006).
- 374 ⁹ C. Pandolfi, D. Izzo, “Biomimetics on seed dispersal: survey and insights for space exploration,”
375 *Bioinspir. Biomim.* 8, 025003 (2013).
- 376 ¹⁰ V. Casseau, G. De Croon, D. Izzo, C. Pandolfi, “Morphologic and aerodynamic considerations
377 regarding the plumed seeds of *tragopogon pratensis* and their implications for seed dispersal,”
378 *PLOS ONE* 10, 1 (2015).
- 379 ¹¹ C. Skupsch, M. Sastuba, and C. Bruecker, “Real time visualization and analysis of sensory hair
380 arrays using fast image processing and proper orthogonal decomposition,” 17th International
381 Symposium on Applications of Laser Techniques to Fluid Mechanics (Lisbon, Portugal, 2014).
- 382 ¹² C. Bruecker, D. Bauer, H. Chaves, “Dynamic response of micro-pillar sensors measuring
383 fluctuating wall-shear-stress,” *Exp. Fluids* 42, 737 (2007).
- 384 ¹³ O. Levin, V. G. Chernoray, L. Loefeldahl, D. S. Henningson, “A study of the blasius wall jet,” *J.*
385 *Fluid Mech.* 539, 313 (2005).
- 386 ¹⁴ C. Resagk, R. du Puits, A. Thess, F. V. Dolzhansky, S. Grossmann, F. F. Araujo, D. Lohse,
387 “Oscillations of the large scale wind in turbulent thermal convection,” *Phys. Fluids* 18, 095105

388 (2006).

389 ¹⁵ R. du Puits, C. Resagk, A. Thess, “Breakdown of wind in turbulent thermal convection,” *Phys.*
390 *Rev. E* 75, 016302 (2007).

391 ¹⁶ F. Ampofo and T. Karayiannis, “Experimental benchmark data for turbulent natural convection
392 in an air filled square cavity,” *Int. J. Heat Mass Transf.* 46, 3551 (2003).

393 ¹⁷ M. Raffel, C. E. Willert, S. Wereley, J. Kompenhans, *Particle Image Velocimetry. A Practical*
394 *Guide* (Springer, Berlin Heidelberg, 2007).

395 ¹⁸ N. Shi, M. S. Emran, J. Schumacher, “Boundary layer structure in turbulent Rayleigh-Bénard
396 convection,” *J. Fluid Mech.* 706, 5 (2012).

397 ¹⁹ S. Kotz and S. Nadarajah, *Extreme Value Distributions Theory and Applications* (Imperial
398 College Press, London, 2000).

399 ²⁰ U. A. Kumar, A. Durga, “Application of extreme value theory in commodity markets,” *Proc.*
400 *of the IEEE International Conference on Industrial Engineering and Engineering Management*
401 867 (2013).

402 ²¹ MATLAB, version 9.0.0.341360 (R2016a) The MathWorks Inc., Natick, Massachusetts.

403 ²² R. du Puits, C. Resagk, A. Thess, “Mean Velocity Profile in Confined Turbulent Convection,”
404 *Phys. Rev. Lett.* 99, 234504 (2007).

405 ²³ D. Funfschilling, G. Ahlers, “Plume motion and large-scale circulation in a cylindrical
406 Rayleigh-Bénard cell,” *Phys. Rev. Lett.* 92, 194502 (2004).

407 ²⁴ H. D. Xi, K. Q. Xia, “Azimuthal motion, reorientation, cessation, and reversal of the
408 large-scale circulation in turbulent thermal convection: a comparative study in aspect ratio one
409 and one-half geometries,” *Phys. Rev. E* 78, 036326 (2008).

410 ²⁵ R. Örlü, P. Schlatter, “On the fluctuating wall-shear stress in zero pressure-gradient turbulent
411 boundary layer flows,”. *Phys. Fluids* 23, 021704 (2011).

412